Broadband White-Light-Emitting Electrochemical Cells

Brando Adranno, Shi Tang, Veronica Paterlini, Volodymyr Smetana, Olivier Renier, Guillaume Bousrez, Ludvig Edman, and Anja-Verena Mudring*

Emerging organic light-emitting devices, such as light-emitting electrochemical cells (LECs), offer a multitude of advantages but currently suffer from that most efficient phosphorescent emitters are based on expensive and rare metals. Herein, it is demonstrated that a rare metal-free salt, bis(benzyltriphenylphosphonium) tetrabromidomanganate(II) ([Ph$_3$PBn]$_2$[MnBr$_4$]), can function as the phosphorescent emitter in an LEC, and that a careful device design results in the fact that such a rare metal-free phosphorescent LEC delivers broadband white emission with a high color rendering index (CRI) of 89. It is further shown that broadband emission is effectuated by an electric-field-driven structural transformation of the original green-light emitter structure into a red-emitting structure.

1. Introduction

Light-emitting electrochemical cells (LECs) have received significant interest since they were first reported by Pei and collaborators in 1995.[1–3] LECs are considered a promising cost-efficient and robust alternative to the more common organic light-emitting diodes (OLEDs), because their simpler and air-stable device structure enables for low-cost printing and coating fabrication under ambient air. Fundamental research has resulted in an improved understanding of the complex LEC working mechanism,[4–6] which in turn has paved the way for devices with increased efficiency, a broader color gamut, and prolonged operational lifetime.[6–8] The most common emitting materials in LECs are conjugated polymers,[6,9–11] small molecules,[12–16] quantum dots,[17–20] and ionic transition metal complexes (iTMCs).[10,21–24] The latter are particularly efficient as spin–orbit coupling (SOC) enables for harvesting of all electrically generated excitons (i.e., both triplets and singlets) for light emission.[25,26] However, a drawback is that they are based on rare and expensive metals, such as iridium, ruthenium, and platinum.[23,24,27–33] Moreover, current iTMC-LECs that combine high efficiency with appreciable lifetime emit in the orange-to-red region of the visible spectrum.[6,24,34–36] Albeit recently progress has been made with LECs based on stable green-emitting Ir(III) complexes,[23,37,38] there are still a lack of stable blue-emitter materials to allow for RGB iTMC-LECs.[30]

For these reasons, alternative emitter materials have to be developed and studied. One of the most promising approaches consists of so-called organic–inorganic hybrid perovskites (HOIPs),[39] which are popular as both solar cell materials and as emissive materials.[40–48] Devices exploiting these types of materials demonstrate rather high performance, but a negative aspect is that they are based on toxic Pb. In this context, it is promising that Pb-free HOIPs have been reported to show good light-emission performance in OLEDs.[49,50] Particularly, Mn-based iTMCs, frequently also addressed as HOIPs, garner interest as the emitting material in OLEDs[51–54] since Mn is Earth abundant and Mn(II) complexes are known to be emissive.[55] To a certain extent, color tuning of the emission of these complexes can be achieved by structural variation.[56] Green-emitting OLEDs based on the emission from tetrahedrally coordinated Mn(II) in [Ph$_4$P]$_2$[MnBr$_4$][51] as well as red-emitting OLEDs based on the emission from octahedric Mn(II) complexes as (ABI)$_4$MnBr$_6$ (ABI = 2-aminobenzimidazole)[53] have been reported. We also note a report on a white-emitting LED based on [C$_9$NH$_{20}$]$_9$[Pb$_3$Br$_{11}$][MnBr$_4$]$_2$ ([C$_9$NH$_{20}$] = N-butyl-N-methylpyrrolidinium), which delivers green emission from the [MnBr$_4$]$^{2-}$ unit, red emission from the [Pb$_3$Br$_{11}$]$^{5-}$ unit, and blue emission from the LED chip.[57] Additionally, a sunlight-like-emitting OLED was prepared utilizing a blend of green-emitting bis(tetraphenylphosphonium) tetrabromidomanganate [Ph$_4$P]$_2$[MnBr$_4$], yellow-emitting [C$_4$N$_2$H$_{14}$Br]$_4$[SnBr$_6$] ([C$_4$N$_2$H$_{14}$Br] = N,N'-dimethylethylene-1,2-diammonium) and red-emitting bis-(tetraphenylphosphonium) pentachloroantimonate [Ph$_4$P]$_2$[SbCl$_5$].[58] However, to our knowledge, broadband white light emission from Mn complexes in LEC devices has not been reported.

B. Adranno, V. Paterlini, V. Smetana, O. Renier, G. Bousrez, A.-V. Mudring
Physical Materials Chemistry
Department of Materials and Environmental Chemistry
Stockholm University
10691 Stockholm, Sweden
E-mail: anja.mudring@rub.de, anja-verena.mudring@mmk.su.se

S. Tang, L. Edman
The Organic Photonics and Electronics Group
Department of Physics
Umeå University
SE- 90187 Umeå, Sweden

V. Smetana, G. Bousrez, A.-V. Mudring
Intelligent Advanced Materials (iAM)
Department of Biological and Chemical Engineering and iNANO
Aarhus University
8000 Aarhus C, Denmark

This inspired us to explore whether Mn-based complexes could be a suitable emitter material for LECs. In particular, we are interested in whether white-emitting LECs could be realized, as it has been recently observed that changes in coordination, achieved by external stimuli, can result in changes in the emission color of Mn complexes.[59] Here we report on the systematic characterization of a recently reported[60] bis(benzyltriphenylphosphonium) tetrabromidomanganate(II) $[Ph_3PBn]_2[MnBr_4]$ for use in LEC devices and demonstrate that an in situ electrical-driven structural transformation enables the attainment of broadband white emission Mn complex-based LEC.

2. Results and Discussion

2.1. Synthesis

$[Ph_3PBn]_2[MnBr_4]$ could be obtained as a whitish powder in a simple one-pot one-day reaction of appropriate amounts of triphenylphosphine (Ph_3P), benzylbromide (BnBr), and manganese bromide ($MnBr_2$) in an acetonitrile (ACN) solution (**Scheme 1**).

2.2. Structural Characterization

Single crystals of $[Ph_3PBn]_2[MnBr_4]$ for single crystal X-ray diffraction (SCXRD) analysis were obtained by slow isothermal evaporation of an acetonitrile solution under ambient conditions. The room-temperature polymorph of $[Ph_3PBn]_2[MnBr_4]$, which recently was reported,[60] crystallizes isotypic with the analogous tetrachloridomanganate(II) $[Ph_3PBn]_2[MnCl_4]$[61] in the triclinic space group $P-1$ ($a = 10.4227(4)$, $b = 12.4158(6)$, $c = 18.2919(9)$, $\alpha = 105.782(2)$, $\beta = 92.969(2)$, $\gamma = 92.759(2)°$, $V = 2270.0(2)$ Å^3, $Z = 2$). Mn(II) is coordinated by four bromide anions in the form of a distorted tetrahedron (Figure S2, Supporting Information). The Mn–Br distances and the Br–Mn–Br angles range between 2.4961(4) and 2.5570(5) Å and between 106.1(1)° and 111.6(1)°, respectively. These values are similar to those reported for $[Ph_4P]_2[MnBr_4]$ (2.5056(7)−2.5070(8) Å and 106.85(2)−111.84(2)°).[51] The $[Ph_3PBn]^+$ cation adopts a pseudotetrahedral structure with C–P–C angles of the central PC4 tetrahedron being similar to the ideal tetrahedral angle 107.0−111.5(1)° (Figure S2, Supporting Information), as commonly observed for similar salts, such as the isotypic $[Ph_3PBn]_2[MnCl_4]$,[61] $[Ph_3PBn][CuCl_2]$, and $[Ph_3PBn][FeCl_4]$.[62] The general packing can be characterized as salt like with preferred cationic–anionic checkered motifs and dominant CH···Br interactions (**Figure 1**). Short Br···H contacts between the anionic center and the cations start from ≈2.8 Å, revealing the presence of weak electrostatic or dispersion interactions.
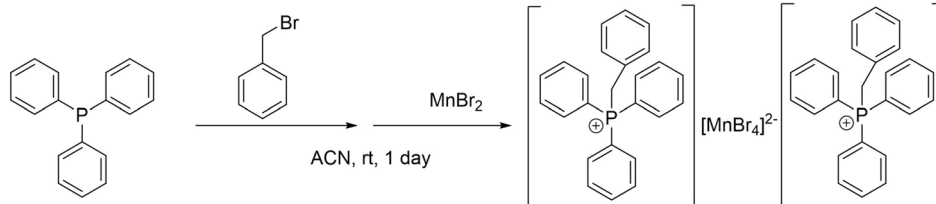
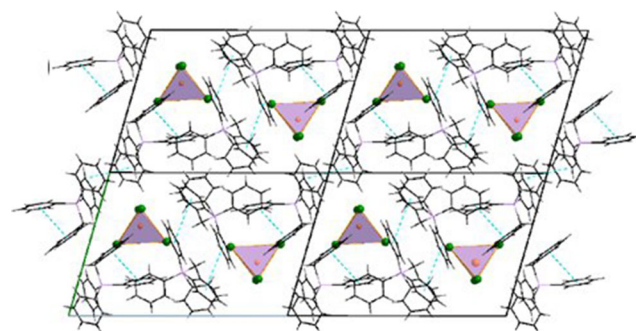**Figure 1.** Molecular packing in the crystal structures of $[Ph_3PBn]_2[MnBr_4]$. The crystallographic axes are color coded: a (red), b (green), and c (blue).

The emissive Mn^{2+} centers are separated, with the closest Mn^{2+}–Mn^{2+} distance being larger than 10 Å.

The powder X-ray diffraction (PXRD) pattern simulated from the SXRD results confirms the phase purity of the obtained product (**Figure 2**). The tetrahedra-like coordination of Mn^{2+} by Br^- was further confirmed by Raman spectroscopy (Figure S4, Supporting Information). $[Ph_3PBn]_2[MnBr_4]$ exhibits a peak at 149 cm^{-1} that corresponds to the symmetric Mn–Br vibration of $[MnBr_4]^{2-}$ (A1 mode). Moreover, the weak shoulder at 235 cm^{-1} is assigned to the symmetric F_2 vibrational mode of a distorted tetrahedron. The observed values are in agreement with what has been reported for tetrabromidomanganates(II) with other organic cations such as dialkylimidazolium, tetraethylammonium, and tetrabutylammonium.[56,63,64] Measurements on $[Ph_3PBn]_2[MnBr_4]$ in the amorphous glassy state (vide infra) showed broader signals and a higher background, as expected for an amorphous material. The symmetric A_1 mode was clearly observable but slightly blueshifted to 153 cm^{-1}. This confirmed that the tetrahedral coordination of Mn^{2+} is preserved in the glassy state.

2.3. Thermal Properties

The thermal properties of $[Ph_3PBn]_2[MnBr_4]$ were investigated by thermogravimetric analysis (TGA), differential scanning calorimetry (DSC), and polarized optical microscopy (POM). The TGA reveals a two-step decomposition (Figure S5, Supporting Information) as observed before.[60] The first decomposition occurs between 311 and 423 °C and results in a 73% mass loss. The second decomposition takes place between 607 and 750 °C and results in a mass loss of 18.5%. The two-step decomposition is similar to what has been observed for tetrabromidomanganates(II) with different organic cations such
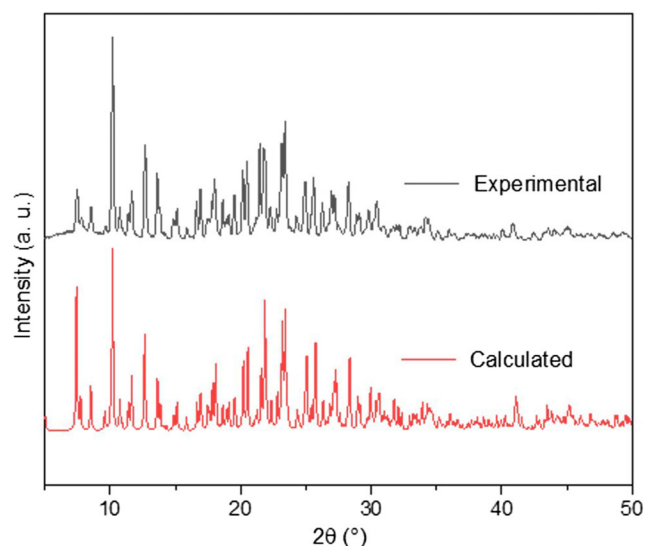

Scheme 1. Synthesis of $[Ph_3PBn]_2[MnBr_4]$.

Figure 2. Comparison of the measured PXRD pattern of [Ph$_3$PBn]$_2$[MnBr$_4$] (black line) with the respective simulated one (red line).

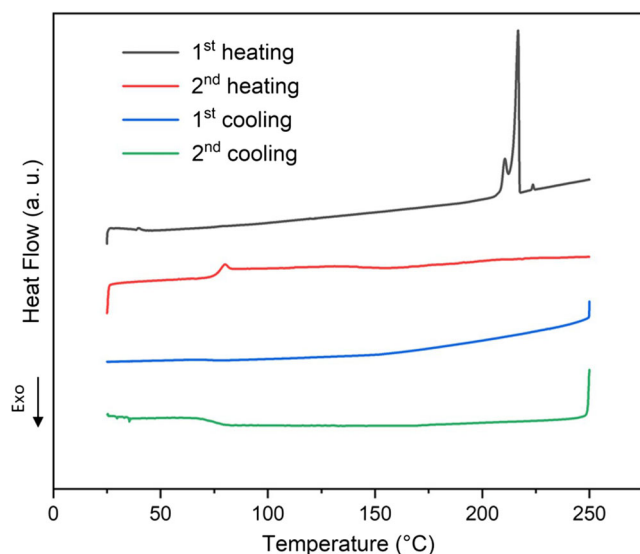**Figure 3.** DSC traces of [Ph$_3$PBn]$_2$[MnBr$_4$]. The features at LT of the first heating cycle and the second cooling cycles are instrument artifacts.

as [Ph$_4$P]$_2$[MnBr$_4$] and [C$_7$H$_{10}$N]$_2$[MnBr$_4$].[51,59,65] Importantly, [Ph$_3$PBn]$_2$[MnBr$_4$] exhibits thermal stability up to 300 °C, which is higher than ammonium relatives such as [Bu$_4$N]$_2$[MnBr$_4$] (first decomposition step at 220 °C),[66] [Pr$_4$N]$_2$[MnBr$_4$] (273 °C), and [Et$_4$N]$_2$[MnBr$_4$] (298 °C)[67] and comparable, or higher, than phosphonium derivatives such as [(H$_2$C CHCH$_2$)(C$_6$H$_5$)$_3$P]$_2$[MnBr$_4$] (273 °C),[54] [C$_{38}$H$_{34}$P$_2$][MnBr$_4$] (310 °C, [C$_{38}$H$_{34}$P$_2$] = ethylenebis-(triphenylphosphonium)),[68] and [Ph$_4$P]$_2$[MnBr$_4$] (<400 °C).[51]

DSC reveals a rather complex temperature-dependent phase behavior. The first DSC heating scan features three endothermic events at 207, 214, and 220 °C (**Figure 3**) with heat contents of 6.29, 49.06, and 0.81 J g^{-1}, respectively. The corresponding entropy changes (ΔS) are 11.7, 90.0, and 1.5 J mol^{-1} K^{-1}. The compound does not recrystallize during the lowering of the temperature in the first cooling scan. Instead, a glass transition is observed with an onset at 78 °C. The corresponding devitrification occurs at 77 °C during the second heating scan, where after no additional phase transition is observed. The following heating–cooling cycles were consistent with the second cycle.

Temperature-dependent POM was used to elucidate the nature of the different phases observed during the first heating scan in DSC (**Figure 4**). During the passage of the first phase transition at 207 °C, [Ph$_3$PBn]$_2$[MnBr$_4$] is observed to remain (poly)crystalline, as revealed by the presence of grains in the pictures collected both below (200 °C) and above (211 °C) the transition temperature. Thus, this transition is associated with a crystal–crystal phase transition. Interestingly, the related compound [Ph$_3$PBn]$_2$[MnCl$_4$] has been reported to form two crystalline structures: triclinic[61] and orthorhombic.[60] Since we observed that [Ph$_3$PBn]$_2$[MnBr$_4$] crystallizes into the triclinic structure at room temperature by evaporation of an acetonitrile solution, we suggest that the first phase transition of [Ph$_3$PBn]$_2$[MnBr$_4$] at 207 °C is between the triclinic and the orthorhombic crystalline structures. However, the stability window for this second polymorph is so narrow that, despite attempts, we could not manage to collect diffraction patterns for the second phase. The second transition at 214 °C should involve a transition to a mesophase, based on the large entropy change of $\Delta S = 90.0$ J mol^{-1} K^{-1} that points to a major loss of order. Although the observed texture of the high-temperature phase under POM confirms the formation of a mesophase, it does not allow for an unambiguous assignment of the mesophase type (Figure 4). The entropy change for the third endothermic event at 220 °C is much lower ($\Delta S = 1.5$ J mol^{-1} K^{-1}), and we assign it to melting into an isotropic liquid, which could be confirmed by POM. Both DSC and POM show that
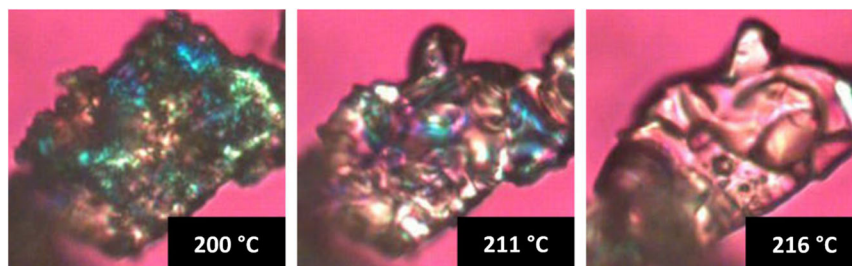

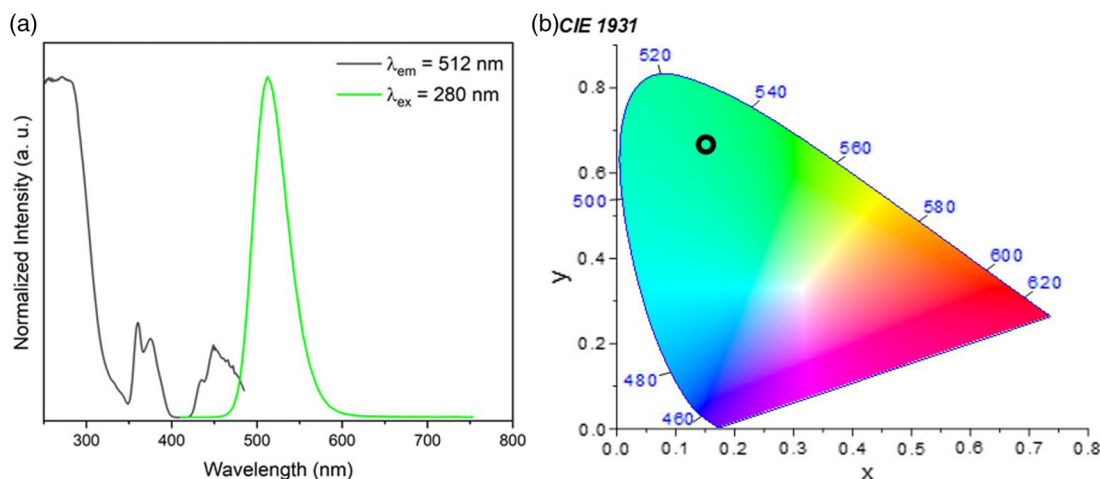**Figure 4.** The morphology of the [Ph$_3$PBn]$_2$[MnBr$_4$] powder, as observed by POM, at the indicated temperatures.

Figure 5. a) Excitation (black) and photoluminescence (green) spectra of [Ph$_3$PBn]$_2$[MnBr$_4$] and b) the corresponding emission coordinates in a CIE 1931 diagram.

Table 1. Photoluminescence properties of [Ph$_3$PBn$_2$[MnBr$_4$].

	λ_{ex} [nm]	λ_{em} [nm]	Φ [%][a]	τRT [µs]	τLT [µs]
[Ph$_3$PBn]$_2$[MnBr$_4$]	280	512	100	304	318
	361	512	46	301	305

[a]QY measurement was possible only at RT due to instrumental limitations.

crystallization upon cooling is strongly suppressed and that the glassy, amorphous phase persists at room temperature. Importantly, this uniform glassy phase morphology is often preferable in thin-film electronic devices, since it suppresses

the risk for short circuits through the active material by the exclusion of crystalline boundaries.

2.4. Photoluminescence

Excitation and emission spectra (**Figure 5**a), as well as emission lifetimes (τ) and emission quantum yields (QYs), were recorded at room temperature (RT), see **Table 1**. The respective Tanabe–Sugano diagram was used for assignment of the electronic transitions.[69] The excitation spectrum of [Ph$_3$PBn]$_2$[MnBr$_4$] exhibits Mn^{2+} bands corresponding to the transitions from the ^{6}A1 state to the ^{4}E(D), ^{4}T$_2$(D) states (350–400 nm) or to the ^{4}A1$_4$E(G), ^{4}T$_2$(G), and ^{4}T$_1$(G) states (420–500 nm). The excitation bands
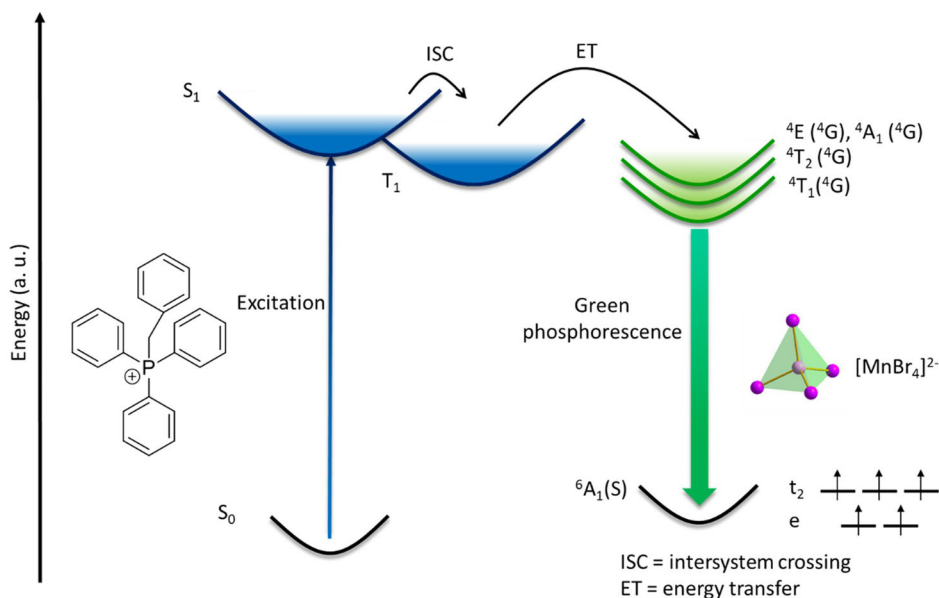

Figure 6. A schematic of the excitation of the organic cations ($\lambda_{ex} = 280$ nm), the energy transfer, and the phosphorescent emission originating from [MnBr$_4$]$^{2-}$ in [Ph$_3$PBn]$_2$[MnBr$_4$].

ADVANCED
SCIENCE NEWS
www.advancedsciencenews.com

ADVANCED
PHOTONICS
RESEARCH
Open Access
www.adpr-journal.com

of the aromatic rings of the cation (as evident by a comparison of the spectra with those reported for [Ph$_3$PBn]Br[70] and to ^{4}T$_2$(F) as well as ^{4}A$_2$(F) of the manganese(II) center overlap in the range between 280 and 400 nm (Figure S6, Supporting Information). With that exception, the spectra are similar to those of bis(tetraalkylammonium)tetrabromidomanganate(II) complexes.[71–75] As expected from tetrahedrally coordinated Mn(II), the RT emission spectrum revealed a green emission band with a maximum at 512 nm (Figure 5). The full width at half maximum (FWHM) is only 46 nm, while the Stokes shift (SS) is large at 231 nm. Interestingly, energy transfer from the organic cation to the [MnBr$_4$]$^{2-}$ centers can be observed, as the excitation spectrum evidences and the emission spectrum confirms (Figure 5a). Thus, upon excitation of the ligand, intersystem crossing (ISC) from the ligand singlet to the triplet state takes place. Thereafter, energy transfer to Mn^{2+} takes place, from which

the radiative emission occurs (**Figure 6**). The photoemission of [Ph$_3$PBn]$_2$[MnBr$_4$] can be fit with a single exponential function, yielding an emissive lifetime of 304 μs. The long lifetime yields supports that the emission is from a triplet state. The QY is close to unity when the organic cation is photoexcited (280 nm). A similar efficient energy transfer process has previously been observed for [Ph$_4$P]$_2$[MnBr$_4$].[51]

Investigations at low temperature (LT = 77 K) did not result in a change in the emission maximum, regardless of whether the photoexcitation was on the cation (λ_{ex} = 280 nm) or on Mn^{2+} (λ_{ex} = 361 nm) (Table 1). However, upon excitation at 280 nm, the compound showed a longer emission lifetime of the excited state of 318 μs at LT compared to 304 μs at RT, which is expected as the phonon-mediated radiationless deactivation is reduced at lower temperature. Since the organic moieties mainly contribute to the higher-energy band, lowering the temperature will hinder
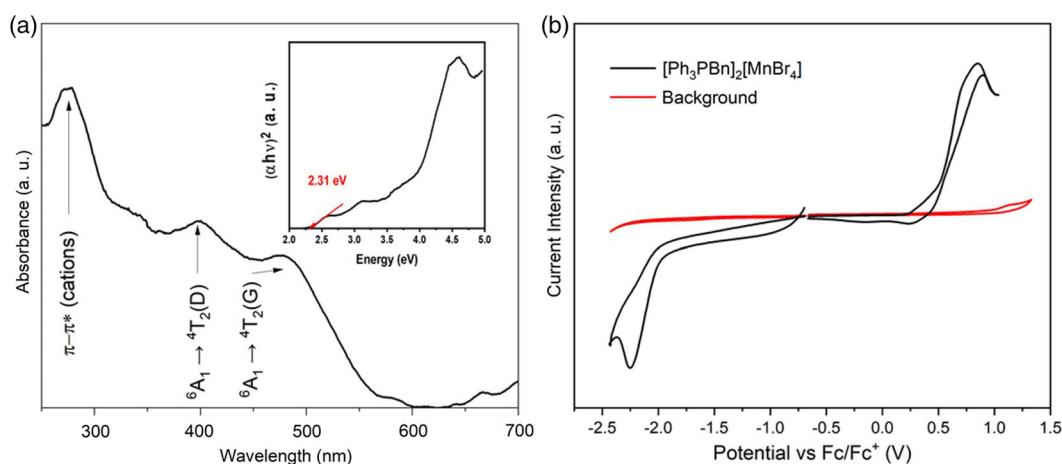
Figure 7. a) The absorption spectrum of the [Ph$_3$PBn]$_2$[MnBr$_4$] powder, with the corresponding Tauc plot as an inset. b) Cyclic voltammogram of [Ph$_3$PBn]$_2$[MnBr$_4$] in ACN solution. The concentration of [Ph$_3$PBn]$_2$[MnBr$_4$] was M. Tetrahexylammonium tetrafluoroborate ([THA][BF4], 0.1 M) was the supporting electrolyte.
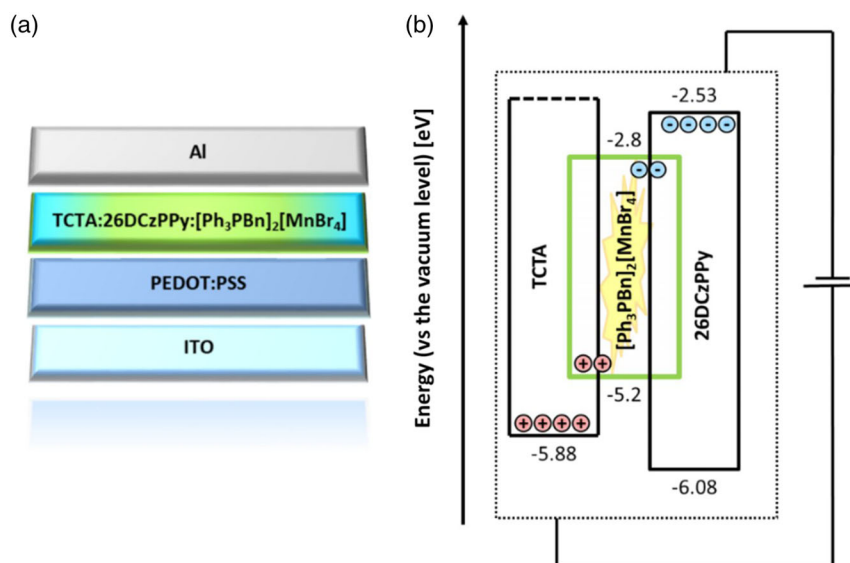
Figure 8. a) The LEC device structure. b) The energy structure of the LEC active material.

**ADVANCED
SCIENCE NEWS**

www.advancedsciencenews.com

**ADVANCED
PHOTONICS
RESEARCH**

www.adpr-journal.com

energy dissipation through vibrational and rotational motions, therefore leading to longer lifetime. In contrast, upon direct excitation into the Mn^{2+} levels, no significant change in lifetimes was observed, which is attributed to the rather rigid environment provided by the halide anions.

2.5. Absorption Spectroscopy and Electrochemical Characterization

Absorption spectra of $[Ph_3PBn]_2[MnBr_4]$ were collected on a crystalline powder (**Figure 7**) and in the glassy state (Figure S7, Supporting Information). The absorption spectrum of the crystalline powder reveals three main features, with the higher-energy part comprising the π–π^* transition on the organic cations (275 nm) and the $^6A_1 \rightarrow {}^4T_2(F)$ and $^6A_1 \rightarrow {}^4A_2(F)$ of Mn^{2+}, while the intermediate-energy part comprises the $^6A_1 \rightarrow {}^4E(D)$ and $^6A_1 \rightarrow {}^4T_2(D)$ ($\approx$400 nm), and the lower-energy part features the $^6A_1 \rightarrow {}^4A_{14}E(G)$; f) $^6A_1 \rightarrow {}^4T_2(G)$; and g) $^6A_1 \rightarrow {}^4T_1(G)$ (475 nm) transitions. The spectrum recorded in the glassy state reveals almost identical features (Figure S7, Supporting Information), supporting that the local environment of Mn^{2+} is largely unaltered. The optical energy gap was determined to be 2.3 eV by replotting the absorption spectrum of the powder sample as a Tauc Plot (see inset in Figure 7a) and using the relationship $\Delta E_\lambda = 1240/\lambda_{\text{onset}}$ (where ΔE_λ is optical bandgap and λ_{onset} the onset of the absorption bands at low energies).

The cyclic voltammetry (CV) investigation of $[Ph_3PBn]_2[MnBr_4]$ in acetonitrile solution revealed oxidation at 0.4 V and reduction at -2.0 V versus Fc/Fc$^+$ (Figure 7b). The onset values for oxidation and reduction can be translated into the highest occupied molecular orbital (HOMO) and lowest unoccupied molecular orbital (LUMO) energy levels, respectively, with the following equation $E_{HOMO(LUMO)} = -(4. + {}_{(Red)})[eV]$ (where $E_{Ox(Red)}$) is the onset of oxidation (reduction) versus the Fc/Fc$^+$ redox couple). This yielded a HOMO level of -5.2 eV and a LUMO level of -2.8 eV with respect to the vacuum level. This resulted in that the electrochemical energy gap is 2.4 eV, which is close to the value for the optical energy gap (2.3 eV).

2.6. Design, Performance, and Evaluation of LECs

The employed LEC device structure is shown in **Figure 8**a. Briefly, a 40 nm-thin PEDOT:PSS layer was spin coated on an indium tin oxide (ITO)-coated glass substrate. The active-material constituents were dissolved in dichloromethane and spin coated as a 140 nm thick dry layer on top of the PEDOT:PSS. The Al top electrode was finally deposited by thermal vacuum evaporation. The detailed composition and the energy structure of the active material is displayed in Figure 8b. We employed tris(4-carbazoyl-9-ylphenyl)amine (TCTA) and 2,6-bis(3-(9H-carba- zol-9-yl)phenyl)pyridine (26DCzPPy) as the hole- and electron-transporting host materials, respectively, in the active material, in line with recent LEC and OLED studies.[51,76] The energy structure of the active material reveals that $[Ph_3PBn]_2[MnBr_4]$ functions as the guest compound on which both electrons and holes can be trapped. We further included the ionic liquid [THA][BF$_4$] as an electrolyte into the active material, since we invariably found that the devices void of it did not deliver light emission. Our conclusion is that the mobilities of the Ph_3PBn^+ cations and the $[MnBr_4]^{2-}$ anions in the active material are too low to allow for a redistribution of ions for the formation of electric-double layers and for the facilitation of electrochemical doping.

The performances of the herein-presented LEC devices are shown in **Table 2**. From the collected data, the best-performing LEC featured a TCTA:26DCzPPy:[THA][BF$_4$] mass ratio of 1:1:0.2, with the $[Ph_3PBn]_2[MnBr_4]$ guest included at either 10 mass% (device termed LEC1) or 20 mass% (LEC2). The presented device results were recorded on LECs driven by a constant

Table 2. Summary of the LEC performance.

Device (% guest)[a]	EL[b] peaks [nm]	CIE [x,y]	CRI[c]	L[d] max [cd m^{-2}]	η[e] [cd A^{-1}]	EQE[f] [%]
LEC1 (10)	440, 525, 625	0.47, 0.37	85	21	0.03	0.021
LEC2 (20)	520, 625	0.43, 0.38	89	46	0.06	0.045

[a]All devices were driven by a constant-current density of 77 mA cm^{-2}; [b]Electroluminescence; [c]CRI; [d]Maximum luminance; [e]Current efficacy; [f]External quantum efficiency.
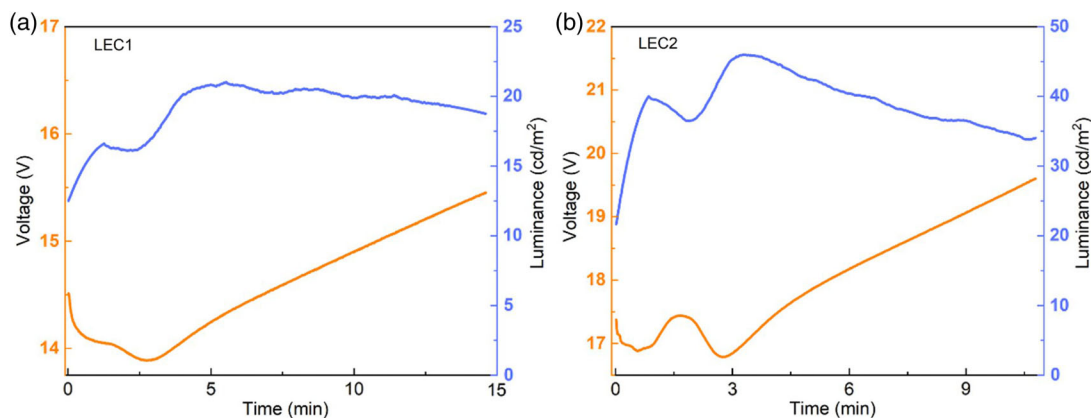

Figure 9. The temporal evolution of the voltage (in orange) and the luminance (in blue) of a) LEC1 and b) LEC2 during driving by a constant current density of 77 mA cm^{-2}.

ADVANCED
SCIENCE NEWS

www.advancedsciencenews.com

ADVANCED
PHOTONICS
RESEARCH
Open Access

www.adpr-journal.com

current density of 77 mA cm^{-2}, with Al biased as the negative cathode.

Figure 9 presents the voltage (left y-axis, orange line) and the luminance (right y-axis, blue line) transients recorded on representative pristine LEC devices during constant-current driving. The initial increase in the luminance and the decrease in voltage result from the redistribution of mobile ions. This results in the formation of electric double layers at the electrode interfaces that enable efficient and balanced electron and hole injection and for the subsequent electrochemical p- and n-type doping of the host and guest compounds. The latter process eventually ends in the in situ formation of a light-emitting p–n junction in the active material. The capability of the [Ph$_3$PBn]$_2$[MnBr$_4$] guest for electrochemical p- and n-type doping is in agreement with its
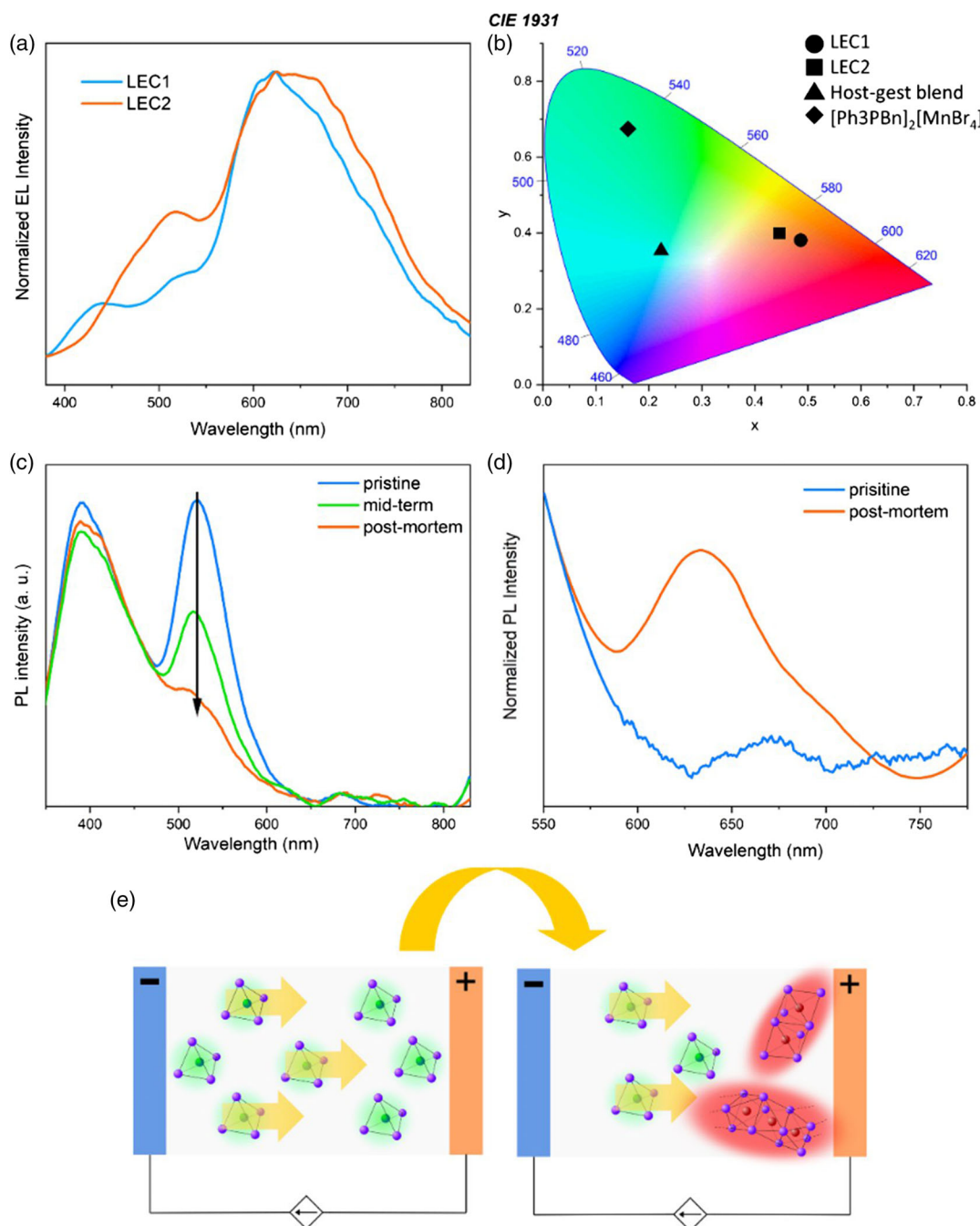
Figure 10. a) Normalized EL spectrum of LEC1 (blue line) and LEC2 (red line). b) Color coordinates of the two broadband emitter LECs within the CIE 1931 diagram. c,d) Photoluminescence spectrum of the active material of LEC2 before LEC operation ("pristine"), at peak luminance ("midterm"), and after the end of LEC operation ("post mortem"). Note that the PL spectra in (c) were excited by $\lambda_{ex} = 300$ nm, while the PL spectra in (d) were excited by $\lambda_{ex} = 475$ nm. e) Proposed mechanism of formation of red-emitting Mn(II) halides complexes.

observed electrochemical oxidation and reduction reactions in the CV experiment (Figure 7b). The progression of these electrochemical doping processes is manifested in that a lower voltage is required to drive a set current through the device, and in that the conversion of the current to light emission becomes more efficient, that is, that the luminance increases with time during constant-current operation.

We find that the lowest voltage is obtained with lower-guest-concentration LEC1 device, whereas a stronger and more efficient luminance is achieved with the higher-guest-concentration LEC2 device. The double maxima in the time-dependent evaluation of luminance are reproducible observations and can be attributed to the movement of the p–n junction during LEC operation.[77] Since the LEC p–n junction is thin and acts within a weak optical microcavity, such a movement will result in that the light generated in the p–n junction will shift between positions of constructive and destructive interference.

Figure 10a presents the electroluminescence (EL) spectra of the two LEC devices at peak luminance, and it is notable that both deliver broadband EL that covers the entire visible regime. These EL spectra were utilized to calculate that the CIE 1931 coordinates are (0.47, 0.37) for LEC1 and (0.43, 0.38) for LEC2 and that the color rendering index (CRI) is 85 for LEC1 and 89 for LEC2. Figure 10b displays the color coordinates in the CIE 1931 diagram. We call attention to that the CRI values are very high and actually comparable with that of commercial metal–halide light sources.[78]

A closer inspection of the EL spectra reveals three broad bands, located in the blue (EL peak = 440 nm), green (EL peak = 525 nm), and red region (EL peak = 625 nm). The blue EL band originates from the TCTA:26DCzPPy blend host (see PL spectrum in Figure S8, Supporting Information).[79,80] When comparing the results for LEC1 and LEC2 it can be seen that the relative magnitude of this band drops with increasing guest concentration, which indicates a more efficient host-to-guest energy transfer. The green EL band stems from the $[Ph_3PBn]_2[MnBr_4]$ guest (see PL spectrum in Figure 5a), while the origin of the lowest-energy red EL band is less clear. An analysis of the energy structure of the active material depicted in Figure 8a excludes the formation of blend-host:guest exciplexes as a plausible cause for red emission. In order to shed light on this intriguing issue, we studied the evolution of the PL for the active material LEC2 device during short breaks during constant-current driving. The PL was excited by either $\lambda_{ex} = 300$ nm (Figure 10c) or $\lambda_{ex} = 475$ nm (Figure 10d), which enabled for separate monitoring of the blue PL and green PL from the blend host and the $[MnBr_4]^{2-}$ complex, respectively (Figure 10c), and the unexpected red PL (Figure 10d). Figure 10c shows that the green PL band drops in relative magnitude during the LEC operation, whereas Figure 10d reveals a corresponding emergence of a red PL band. Thus, the overall spectral effect of the LEC operation is that parts of the green emission are replaced by red emission. It thus appears feasible that the LEC operation provoked a transformation of the characteristic green-emitting $[MnBr_4]^{2-}$ tetrahedra into a red-emitting species. We propose that this green-to-red transformation is due to that the original green-emitting $[MnBr_4]^{2-}$ tetrahedra are transformed into red-emitting Mn(II) octahedra or trigonal bipyramids, which are known to emit red light.[81,82] This structural transformation is driven by the applied electric field and results in that neighboring $[MnBr_4]^{2-}$ units are brought in close contact so that they can form polymeric chains via sharing of Br- ions (Figure 10e). A similar transition from solely green emission to a combination of green and red emission was observed for $[(CH_3)_4N]_2[MnCl_4]$ and $[(CH_3)_4N]_2[MnBr_4]$ crystals during exposure to high pressure,[83] which was attributed to the conversion of $[MnX_4]^{2-}$ complexes into $[MnX_6]^{4-}$ (X = Cl or Br) complexes. Similarly, the conversion of isolated tetrahedral $[MnBr_4]^{2-}$ complexes into chains of face-sharing octahedra $[MnBr_3]^-$ upon transformation to a liquid-crystalline mesophase was reported for a set of 1-alkyl-3-vinyl-imidazolium tetrahalidomanganate(II).[59]

3. Conclusion

A green-emitting $[Ph_3PBn]_2[MnBr_4]$ complex has been synthesized through a new one-step procedure and explored as the principle emitter in LEC devices. By combining this novel emitter with an appropriate blend host and an ionic liquid electrolyte, we were able to realize LEC devices with air-stable electrodes that delivered broadband white emission with a high CRI of 89. A corresponding systematic investigation revealed that the broadband emission comprised three emissive constituents: a high-energy blue emission originating from the blend host, an intermediate-energy green emission from the $[Ph_3PBn]_2[MnBr_4]$ complex, and an unexpected low-energy red emission that appears to stem from structurally reformed Mn complexes. The latter results from a partial conversion of the original green-emitting $[MnBr_4]^{2-}$ tetrahedral complexes to red-emitting octahedral or trigonal bipyramidal Mn(II) complexes during the exposure to an electric current. Our study thus introduces a novel rare-metal-free emitter that could enable realization of practical and low-cost organic electroluminescent devices.

4. Experimental Section

All starting materials were purchased from Sigma Aldrich (Steinheim, Germany) and used without further purification.

Synthesis of bis(benzyltriphenylphosphonium)tetrabromomanganate(II), [Ph₃PBn]₂[MnBr₄]: Benzylbromide (4 mmol, 2 eq.) was added under stirring at room temperature to a solution of triphenylphosphine (4 mmol, 2 eq.) in acetonitrile (50 mL), followed by addition of $MnBr_2$ (2 mmol, 1 eq.). After stirring for one day, the solvent was removed under reduced pressure yielding $[Ph_3PBn]_2[MnBr_4]$ whitish powder. For purification, the salt was recrystallized from acetonitrile.

$[Ph_3PBn]_2[MnBr_4]$: ESI-MS : m/z (negative mode, $[MnBr_4]^{2-}$) 188.445 (calculated m/z = 187.3042).

FTIR: ν_{max} (cm^{-1}) = 3036, 3057, 3007, 2964, 2946, 2918, 2902, 2874, 1585, 1484, 1399, 1437, 1334, 1312, 1247, 1189, 1148, 1160, 1136, 1070, 1108, 1027, 996, 915, 929, 857, 836, 784, 746, 717, 686, 618, 584, 493, 452, 440, 382.

Fourier Transform Infrared Spectroscopy (FTIR): FTIR spectra were collected with a Bruker Alpha-P ATR-spectrometer (Karlsruhe, Germany) in an attenuated total reflection configuration. Data evaluation was carried out with the program OPUS (Bruker, Karlsruhe, Germany).

Raman Spectroscopy: RT Raman spectra ranging from 100 to 4000 cm^{-1} were recorded with a Horiba LabRAM HR system equipped with a CCD detector (Horiba, Japan) using a red laser ($\lambda = 785$ nm). A Si standard (520.5 cm^{-1} line) was used for calibration.

Mass Spectrometry: A SYNAPT G2-S HDMS Q-ToF mass spectrometer (Waters, Manchester, UK) was operated in the positive- and negative-ion

ESI mode with a capillary voltage: 2500 V; extractor: 1.0 V; RF lens: 0.5 V; ion source temperature: 120 °C; and desolvation temperature 250 °C. Nitrogen was used as both the cone and desolvation gas at a flow of 70 and 500 L h^{-1}, respectively. Argon was used as a collision gas at a pressure of 2.95×10^{-4} mbar.

Thermal Characterization: DSC was performed with a computer-controlled LT^{3+} thermal analyzer (Mettler Toledo, Columbus, US). Measurements were carried out at a heating rate of 1 °C min^{-1} with an argon flow rate of 40 mL min^{-1}. The samples were prepared in air and placed in aluminum pans which were cold sealed and punctured. Given temperatures corresponded to the onset of the respective thermal process.

TGA was performed with a TG 449 F3 Jupiter (Netzsch, Selb, Germany), using aluminum oxide crucibles with a heating rate of 10 °C min^{-1} and nitrogen as a purge gas. Given temperatures corresponded to the 5% onset of the respective thermal process.

Polarized Optical Microscopy (POM): Optical analyses were made by heated-stage POM with an Axio Imager A1 microscope (Carl Zeiss MicroImagingGmbH, Göttingen, Germany) equipped with a hot stage, THMS600 (Linkam Scientific Instruments Ltd, Surrey, UK), and Linkam TMS 94 temperature controller. Images were recorded at a magnification of 50× as a video with a digital camera. Heating and cooling rates were 1 °C min^{-1}.

Single Crystal X-ray Diffraction: SCXRD data of [Ph$_3$PBn]$_2$[MnBr$_4$] were recorded using a Bruker D8 Venture (Mo Kα, $\lambda = 0.7093$ Å at 293 K). Data reduction was performed with the program package X-Red or SAINT and absorption corrections were carried out with the programs X-Shape or SADABS. Crystal structure solution was carried out using SHELXT[84] within Olex2.[85] Refinement was performed with SHELXL.[84] Hydrogen atoms were added and treated with the riding atom mode. To illustrate the crystal structures, the programs Diamond[86] and Mercury[87] were used. CCDC 2 115 614 contains the supplementary crystallographic data for this article. These data can be obtained free of charge from The Cambridge Crystallographic Data Centre (CCDC) via www.ccdc.cam.ac.uk/data_request/cif.

Powder X-ray Diffraction: Powder X-ray diffraction (PXRD): Data were recorded at ambient temperature on a PANalytical X'pert PRO diffractometer (Malvern Panalytical, Malvern, UK), operating at 45 kV and 40 mA and using Cu Kα1 radiation ($\lambda = 1.5406$ Å at 293 K). The data was recorded in reflection mode from 5° to 50° with a rate of 0.55 s step^{-1}. The intensity data were integrated and converted with the APEX3 software (Bruker, 2016). Predicted PXRD diffractograms were calculated using Mercury.[87]

Absorption Spectroscopy: The UV–vis absorption spectra on the crystal-line powder and the glassy state of [Ph$_3$PBn]$_2$[MnBr$_4$] were recorded using an Agilent Technologies Cary 5000 UV−Vis−NIR spectrophotometer equipped with an Agilent Praying Mantis diffuse reflectance accessory (Agilent Technologies, Sana Clara, US). A Spectralon disk was used as the reference material for measurements on powder. The glassy state was obtained by cooling the melt of [Ph$_3$PBn]$_2$[MnBr$_4$] to room temperature (as confirmed by PXRD analysis) and then it was crushed into fine powder to fill the sample holder of the spectrophotometer. The spectrum of the 10^{-5} M solution in dichloromethane was recorded on the same instrument in transmission mode, using quartz vials. The pure solvent was utilized as the reference for the measurement.

Photoluminescence: Steady-state excitation, emission spectra, and decay curves were recorded on a HORIBA Jobin Yvon FluoroLog-3 modular spectrofluorometer with an R928P PMT detector (Horiba France, Longjumeau, France). A 450 W xenon arc lamp was used for the steady-state measurements, whereas a pulsed Xe lamp with the instrument operating in a TCPS mode was used for lifetime measurements. QYs were determined on quartz capillary with a sample filled with GMP G8 integrating sphere (MGP, Zurich, Switzerland) using BaSO4 as a reference.

Electrochemistry: Cyclic voltammetry analysis was conducted on a Metrohm Autolab potentiostat driven by the GPES software (Herisau, Switzerland) via the three-electrode method. A Pd disk ($d = 5$ mm) was used as a working electrode, a Pt rod as a counter electrode, and Ag wire as a quasireference electrode. Multiple scans were conducted at 50 mV s^{-1} on a 10^{-3} M solution of [Ph$_3$PBn]$_2$[MnBr$_4$] in acetonitrile. 10^{-1} M

[THA][BF$_4$] was used as an additional electrolyte. Directly after each CV scan, a calibration scan was run with a small amount of ferrocene added to the electrolyte solution. All CV potentials were reported versus the ferrocene/ferrocenium (Fc/Fc$^+$) reference potential. The reduction/oxidation onset potentials were defined as the inter-section of the baseline with the tangent of the current at half-peak height. The CV sample preparation and characterization were executed in a N$_2$-filled glovebox ([O$_2$] < 0.1 ppm, [H$_2$O] < 1 ppm).

Device Fabrication and Characterization: The host compounds tris(4-carbazoyl-9-ylphenyl)amine (TCTA, Lumtec) and 2,6-bis(3-(9Hcarbazol-9-yl)pyridine (26DCzPPy, Lumtec) were dissolved in anhydrous dichloromethane at a concentration of 10 g L^{-1} with a mass ratio of 1:1 under stirring on a magnetic hot plate at 50 °C for >2 h. The host–guest blend were prepared by adding the [Ph$_3$PBn]$_2$[MnBr$_4$] into the host solution in a desired mass ratio, followed by stirring on the magnetic hot plate at 50 °C for >2 h. The active material inks were prepared by adding tetrahexylammonium tetrafluoroborate ([THA][BF$_4$]) ionic liquid into the host–guest blend with a mass ratio of 10:1. Carefully cleaned indium tin oxide (ITO)-coated glass substrates (20 Ω sq^{-1}, Thin Film Devices) were spun coated with a poly(3,4-ethylenedioxythiophene):poly(styrene sulfonate) (PEDOT:PSS) ink (Clevios P VP AI 4083, Heraeus) at 4000 rpm for 60 s and thereafter dried at 120 °C for 30 min. The dry PEDOT:PSS layer was spin coated with the active-material ink at 2000 rpm for 60 s and thereafter dried at 50 °C for 10 min. The dry thickness of the PEDOT:PSS and the active material layers was 40 nm and 140 nm, respectively, as measured with a profilometer (DekTak XT, Bruker). Finally, a set of 100 nm-thick Al cathodes were deposited on top of the active material by thermal vacuum evaporation at $p < 5 \times 10^{-6}$ mbar. The light-emission area, as defined by the size of the cathode, was 0.85×0.15 cm^2. The LEC devices were measured with a computer-controlled source measure unit (Agilent U2722A) and a calibrated photodiode, equipped with an eye-response filter (Hamamatsu Photonics), and connected to a data acquisition card (National Instruments USB-6009) via a current-to-voltage amplifier. The EL spectrum was measured with a calibrated spectrometer (USB2000+, Ocean Optics). All of the above procedures, with the exception of the deposition of PEDOT:PSS, were carried out in two interconnected N2-filled gloveboxes ([O$_2$] < 2 ppm, [H$_2$O] < 1 ppm).

Supporting Information

Supporting Information is available from the Wiley Online Library or from the author.

Conflict of Interest

The authors declare no conflict of interest.

Data Availability Statement

CCDC 2115614 contains the supplementary crystallographic data for this paper. These data can be obtained free of charge from The CCDC via www.ccdc.cam.ac.uk/data_request/cif. Other data can be retrieved from the corresponding author upon request.

Keywords

[1] Q. Pei, G. Yu, C. Zhang, Y. Yang, A. J. Heeger, *Science* **1995**, *269*, 1086.

[2] Q. Pei, Y. Yang, G. Yu, C. Zhang, A. J. Heeger, *J. Am. Chem. Soc.* **1996**, *118*, 3922.

[3] L. D. Bastatas, K.-Y. Lin, M. D. Moore, K. J. Suhr, M. H. Bowler, Y. Shen, B. J. Holliday, J. D. Slinker, *Langmuir* **2016**, *32*, 9468.

[4] S. van Reenen, P. Matyba, A. Dzwilewski, R. A. J. Janssen, L. Edman, M. Kemerink, *J. Am. Chem. Soc.* **2010**, *132*, 13776.

[5] E. Fresta, R. D. Costa, *J. Mater. Chem. C* **2017**, *5*, 5643.

[6] S. Tang, L. Edman, *Top. Curr. Chem.* **2017**, *375*.

[7] J. Gao, *ChemPlusChem* **2018**, *83*, 183.

[8] L. Mardegan, C. Dreessen, M. Sessolo, D. Tordera, H. J. Bolink, *Adv. Funct. Mater.* **2021**, *31*, 2104249.

[9] Z. Yu, L. Li, H. Gao, Q. Pei, *Sci. China Chem.* **2013**, *56*, 1075.

[10] H. C. Su, C. Y. Cheng, *Isr. J. Chem.* **2014**, *54*, 855.

[11] P. Lundberg, Q. Wei, Z. Ge, B. Voit, S. Reineke, L. Edman, *J. Phys. Chem. Lett.* **2020**, *11*, 6227.

[12] Z. B. Hill, D. B. Rodovsky, J. M. Leger, G. P. Bartholomew, *Chem. Commun.* **2008**, 6594.

[13] J. Choi, S. Kanagaraj, Y. Choe, *J. Mater. Chem. C* **2020**, *8*, 4580.

[14] T. Zhang, R. Xu, H. Lv, Z. Wang, H. Ye, H. Liu, L. Chen, *Optik* **2022**, *261*, 169176.

[15] H.-L. Shen, P.-W. Hsiao, R.-H. Yi, Y.-H. Su, Y. Chen, C.-W. Lu, H.-C. Su, *Dyes Pigm.* **2022**, *203*, 110346.

[16] A. Puthanveedu, K. Shanmugasundaram, S. Yoon, Y. Choe, *J. Mater. Chem. C* **2022**, *10*, 2245.

[17] A. J. Norell Bader, A. A. Ilkevich, I. V. Kosilkin, J. M. Leger, *Nano Lett.* **2011**, *11*, 461.

[18] G. Qian, Y. Lin, G. Wantz, A. R. Davis, K. R. Carter, J. J. Watkins, *Adv. Funct. Mater.* **2014**, *24*, 4484.

[19] E. Nannen, J. Frohleiks, S. Gellner, *Adv. Funct. Mater.* **2020**, *30*, 1907349.

[20] Y. Liu, S. Tang, X. Wu, N. Boulanger, E. Gracia-Espino, T. Wågberg, L. Edman, J. Wang, *Nano Res.* **2022**, *15*, 5610.

[21] R. D. Costa, E. Ortí, H. J. J. P. Bolink, *Appl. Chem.* **2011**, *83*, 2115.

[22] R. D. Costa, E. Ortí, H. J. Bolink, F. Monti, G. Accorsi, N. Armaroli, *Angew. Chem., Int. Ed. Eng.* **2012**, *51*, 8178.

[23] J. E. Namanga, H. Pei, G. Bousrez, B. Mallick, V. Smetana, N. Gerlitzki, A. V. Mudring, *Adv. Funct. Mater.* **2020**, *30*, 1909809.

[24] J. E. Namanga, H. Pei, G. Bousrez, V. Smetana, N. Gerlitzki, A.-V. Mudring, *ACS Appl. Energy Mater.* **2020**, *3*, 9271.

[25] H. Yersin, in *Transition Metal and Rare Earth Compounds: Excited States, Transitions, Interactions III* (Ed: H. Yersin), Springer Berlin Heidelberg, Berlin, Heidelberg **2004**.

[26] K. Li, Y. Chen, J. Wang, C. Yang, *Coord. Chem. Rev.* **2021**, *433*, 213755.

[27] C. Cebrián, M. Mauro, *Beilstein J. Org. Chem.* **2018**, *14*, 1459.

[28] Q. Li, C. Shi, M. Huang, X. Wei, H. Yan, C. Yang, A. Yuan, *Chem. Sci.* **2019**, *10*, 3257.

[29] H. Shin, Y. H. Ha, H. G. Kim, R. Kim, S. K. Kwon, Y. H. Kim, J. J. Kim, *Adv. Mater.* **2019**, *31*, 1808102.

[30] R. Bai, X. Meng, X. Wang, L. He, *Adv. Funct. Mater.* **2020**, *30*, 1907169.

[31] C. Zhang, R. Liu, D. Zhang, L. Duan, *Adv. Funct. Mater.* **2020**, *30*, 1907156.

[32] K. Schlingman, Y. Chen, R. S. Carmichael, T. B. Carmichael, *Adv. Mater.* **2021**, *33*, 2006863.

[33] G. Hong, X. Gan, C. Leonhardt, Z. Zhang, J. Seibert, J. M. Busch, S. Bräse, *Adv. Mater.* **2021**, *33*, 2005630.

[34] J. Zhang, L. Zhou, H. A. Al-Attar, K. Shao, L. Wang, D. Zhu, Z. Su, M. R. Bryce, A. P. Monkman, *Adv. Funct. Mater.* **2013**, *23*, 4667.

[35] C. D. Ertl, C. Momblona, A. Pertegás, J. M. Junquera-Hernández, M.-G. La-Placa, A. Prescimone, E. Ortí, C. E. Housecroft, E. C. Constable, H. J. Bolink, *J. Am. Chem. Soc.* **2017**, *139*, 3237.

[36] A. Bonfiglio, P.-W. Hsiao, Y. Chen, C. Gourlaouen, Q. Marchand, V. César, S. Bellemin- Laponnaz, Y.-X. Wang, C.-W. Lu, C. Daniel, F. Polo, H.-C. Su, M. Mauro, *Chem. Mater.* **2022**, *34*, 1756.

[37] M. K. Nazeeruddin, R. T. Wegh, Z. Zhou, C. Klein, Q. Wang, F. De Angelis, S. Fantacci, M. Grätzel, *Inorg. Chem.* **2006**, *45*, 9245.

[38] R. Yu, Y. Song, M. Chen, L. He, *Dalton Trans.* **2021**, *50*, 8084.

[39] H. Lin, C. Zhou, Y. Tian, T. Siegrist, B. Ma, *ACS Energy Lett.* **2018**, *3*, 54.

[40] M. F. Aygüler, M. D. Weber, B. M. Puscher, D. D. Medina, P. Docampo, R. D. Costa, *J. Phys. Chem. C* **2015**, *119*, 12047.

[41] H. Zhang, H. Lin, C. Liang, H. Liu, J. Liang, Y. Zhao, W. Zhang, M. Sun, W. Xiao, H. Li, S. Polizzi, D. Li, F. Zhang, Z. He, W. C. H. Choy, *Adv. Funct. Mater.* **2015**, *25*, 7226.

[42] Z. Yuan, C. Zhou, Y. Tian, Y. Shu, J. Messier, J. C. Wang, L. J. Van De Burgt, K. Kountouriotis, Y. Xin, E. Holt, *Nat. Commun.* **2017**, *8*, 14051.

[43] M. Alahbakhshi, A. Mishra, R. Haroldson, A. Ishteev, J. Moon, Q. Gu, J. D. Slinker, A. A. Zakhidov, *ACS Energy Lett.* **2019**, *4*, 2922.

[44] K. Matsuki, J. Pu, T. Takenobu, *Adv. Funct. Mater.* **2020**, *30*, 1908641.

[45] A. Mishra, S. DiLuzio, M. Alahbakhshi, A. C. Adams, M. H. Bowler, J. Moon, Q. Gu, A. A. Zakhidov, S. Bernhard, J. D. Slinker, *Chem. Mater.* **2021**, *33*, 1201.

[46] A. Mishra, M. Alahbakhshi, R. Haroldson, Q. Gu, A. A. Zakhidov, J. D. Slinker, *Adv. Funct. Mater.* **2021**, *31*, 2102006.

[47] W.-L. Kang, Y.-T. Tsai, Y.-C. Ji, R.-H. Yi, Y.-X. Wang, H.-L. Shen, X.-J. Chen, Y.-C. Hsu, C.-W. Lu, Z.-P. Yang, H.-C. Su, *Chem. Eur. J.* **2021**, *27*, 17785.

[48] A. Mishra, R. Bose, Y. Zheng, W. Xu, R. McMullen, A. B. Mehta, M. J. Kim, J. W. P. Hsu, A. V. Malko, J. D. Slinker, *Adv. Mater.* **2022**, *34*, 2203226.

[49] H. Liang, F. Yuan, A. Johnston, C. Gao, H. Choubisa, Y. Gao, Y. K. Wang, L. K. Sagar, B. Sun, P. Li, *Adv. Sci.* **2020**, *7*, 1903213.

[50] X. Li, X. Gao, X. Zhang, X. Shen, M. Lu, J. Wu, Z. Shi, V. L. Colvin, J. Hu, X. Bai, *Adv. Sci.* **2021**, *8*, 2003334.

[51] L.-J. Xu, C.-Z. Sun, H. Xiao, Y. Wu, Z.-N. Chen, *Adv. Mater.* **2017**, *29*, 1605739.

[52] Y. Qin, P. Tao, L. Gao, P. She, S. Liu, X. Li, F. Li, H. Wang, Q. Zhao, Y. Miao, W. Huang, *Adv. Opt. Mater.* **2019**, *7*, 1801160.

[53] S. Yan, W. Tian, H. Chen, K. Tang, T. Lin, G. Zhong, L. Qiu, X. Pan, W. Wang, *Adv. Funct. Mater.* **2021**, *31*, 2100855.

[54] A. Jana, V. G. Sree, Q. Ba, S. C. Cho, S. U. Lee, S. Cho, Y. Jo, A. Meena, H. Kim, H. Im, *J. Mater. Chem. C* **2021**, *9*, 11314.

[55] Y. Qin, P. She, X. Huang, W. Huang, Q. Zhao, *Coord. Chem. Rev.* **2020**, *416*, 213331.

[56] S. Pitula, A.-V. Mudring, *Chem. Eur. J.* **2010**, *16*, 3355.

[57] M. Li, J. Zhou, G. Zhou, M. S. Molokeev, J. Zhao, V. Morad, M. V. Kovalenko, Z. Xia, *Angew. Chem. Int. Ed.* **2019**, *58*, 18670.

[58] M. Worku, Y. Tian, C. Zhou, S. Lee, Q. Meisner, Y. Zhou, B. Ma, *ACS Appl. Mater. Interfaces* **2018**, *10*, 30051.

[59] Z. Huang, M. Yi, M. Xu, P. Qi, Y. Liu, A. Song, J. Hao, *J. Mater. Chem. C* **2021**, *9*, 13276.

[60] Y. Qin, P. She, S. Guo, X. Huang, S. Liu, Q. Zhao, W. Huang, *Acta Phys. Chim. Sin.* **2020**, *36*, 1907078.

[61] W.-Q. Chen, D.-D. Zhou, M.-H. Feng, Y.-Q. Peng, S. Han, X. Chen, X.-P. Liu, L.-M. Yang, J.-R. Zhou, C.-L. Ni, *Synth. React. Inorg. Met.-Org. Nano-Met. Chem.* **2012**, *42*, 857.

[62] A. A. Hafiz, *J. Iran. Chem. Soc.* **2008**, *5*, 106.

[63] J. S. Avery, C. D. Burbridge, D. M. L. Goodgame, *Spectrochim. Acta, Part A* **1968**, *24*, 1721.

[64] H. Edwards, M. Ware, L. Woodward, *Chem. Commun.* **1968**, 540.

[65] L. Li, L. Li, Q. Li, Y. Shen, S. Pan, J. Pan, *Transition Met. Chem.* **2020**, *45*, 413.

[66] A. Jana, S. Zhumagali, Q. Ba, A. S. Nissimagoudar, K. S. Kim, *J. Mater. Chem. A* **2019**, *7*, 26504.

[67] S. Chen, J. Gao, J. Chang, Y. Zhang, L. Feng, *Sens. Actuators, B* **2019**, *297*, 126701.

[68] L.-J. Xu, X. Lin, Q. He, M. Worku, B. Ma, *Nat. Commun.* **2020**, *11*, 4329.

[69] Y. Tanabe, S. Sugano, *J. Phys. Soc. Jpn.* **1954**, *9*, 766.

[70] T. Li, Z.-H. Gan, C.-H. Liu, J.-R. Zhou, X.-P. Liu, L.-M. Yang, C.-L. Ni, *J. Mol. Struct.* **2019**, *1180*, 163.

[71] C. Furlani, A. Furlani, *J. Inorg. Nucl. Chem.* **1961**, *19*, 51.

[72] F. A. Cotton, D. M. L. Goodgame, M. Goodgame, *J. Am. Chem. Soc.* **1962**, *84*, 167.

[73] A. Mehra, P. Venkateswarlu, *J. Chem. Phys.* **1966**, *45*, 3381.

[74] M. T. Vala, C. J. Ballhausen, R. Dingle, S. L. Holt, *Mol. Phys.* **1972**, *23*, 217.

[75] N. Islam, *J. Appl. Spectrosc.* **1975**, *29*, 266.

[76] S. Tang, P. Lundberg, Y. Tsuchiya, J. Ràfols-Ribé, Y. Liu, J. Wang, C. Adachi, L. Edman, *Adv. Funct. Mater.* **2022**, *32*, 2205967.

[77] J. Ràfols-Ribé, X. Zhang, C. Larsen, P. Lundberg, E. M. Lindh, C. T. Mai, J. Mindemark, E. Gracia-Espino, L. Edman, *Adv. Mater. Processes* **2022**, *34*, 2107849.

[78] M. F. Hordeski, *Dictionary of Energy Efficiency Technologies*, The Fairmont Press, Inc., West Virgina, USA **2004**.

[79] Y. Kuwabara, H. Ogawa, H. Inada, N. Noma, Y. Shirota, *Adv. Mater. Processes* **1994**, *6*, 677.

[80] S.-J. Su, H. Sasabe, T. Takeda, J. Kido, *Chem. Mater.* **2008**, *20*, 1691.

[81] L. Mai, Bachelor Thesis (Supervisor: A.-V. Mudring) Ruhr-Universität Bochum, Bochum, Germany **2014**.

[82] Z.-X. Wang, P.-F. Li, W.-Q. Liao, Y. Tang, H.-Y. Ye, Y. Zhang, *Chem. Asian J.* **2016**, *11*, 981.

[83] Y. Rodríguez-Lazcano, L. Nataf, F. Rodríguez, *Phys. Rev. B: Condens. Matter* **2009**, *80*, 085115.

[84] G. Sheldrick, *Acta Crystallogr., Sect. A: Found. Adv.* **2015**, *71*, 3.

[85] O. V. Dolomanov, L. J. Bourhis, R. J. Gildea, J. A. K. Howard, H. Puschmann, *J. Appl. Crystallogr.* **2009**, *42*, 339.

[86] K. Brandenburg, H. Putz, *Cryst. Impact* **2011**.

[87] C. F. Macrae, I. Sovago, S. J. Cottrell, P. T. A. Galek, P. McCabe, E. Pidcock, M. Platings, G. P. Shields, J. S. Stevens, M. Towler, P. A. Wood, *J. Appl. Crystallogr.* **2020**, *53*, 226.